ORIGINAL ARTICLE   **Open Access**

Microstructures, Thermal and Mechanical Properties of Pure Tungsten—A Comparison Between Selective Laser Melting and Hot Rolling

Chong Wang[1], Daobing Chen[1], Yan Zhou[2*], Zhuoming Xie[3], Qianfeng Fang[3], Shifeng Wen[1*] and Chunze Yan[1]

Abstract

A comparative study on the influence of different manufacturing methods (selective laser melting and hot rolling) on the microstructure, mechanical and thermal behaviours of tungsten (W) was presented for the first time. The results indicated that the selective laser melting (SLM) W exhibited a finer grain sizes, a lower strength ductility, hardness and thermal conductivity compared to hot-rolled W. The main reason for this result was that the laser underwent rapid heating and cooling when it was used to melt W powder with high energy density, resulting in large internal stress in the sample after manufacturing. Subsequently, the internal stress was released, leading to the generation of micro-cracks at the grain boundaries, thereby affecting the performance of SLM W samples. In addition, the higher fraction of high-angle grain boundaries (HAGBs) of SLM W was found to be the key factor for intrinsic brittleness. Because the HAGBs are the preferred crack paths, which could promote crack propagation and decrease fracture energy.

Keywords: Tungsten (W), Selective laser melting (SLM), Hot rolling, Microstructure, Thermal conductivity, Mechanical property

1 Introduction

Tungsten (W), a typical refractory metal, has high melting point, low thermal expansion coefficient, low tritium retention and high self-sputtering threshold [1]. Due to these characteristics, pure W has been widely used as plasma facing materials (PFMs) in fusion devices [2]. W is generally considered as a brittle material at room temperature because of its high ductile-brittle transition temperature (DBTT). Consequently, W has always been fabricated primarily using the powder metallurgy (PM) method [3]. The pressed powder is sintered and generally deformed (forged, rolled, drawn, etc.) under high temperature to produce the final products (billets, bars, plates, etc.) [4–6]. However, the PM method has a limitation in terms of the production of parts with complex geometries, such as He-cooled divertor in fusion reactors [7]. Therefore, it is necessary to find a novel approach to fabricate W parts with intricate structures to expand the application scope.

Selective laser melting (SLM) is one of the promising additive manufacturing techniques. During the SLM process, a fiber laser works as the energy source for melting and solidifying the metal powders of selected areas according to the CAD data. Then the substrate is lowered and the laser repeats to scan and deposit next layer until the whole parts are fabricated [8, 9]. The SLM exhibits considerable advantages in fabricating metal parts with desired complex shapes [10, 11]. Recently, SLM has been widely applied in preparing

---

*Correspondence: zhouyan@cug.edu.cn; roya_wen@hust.edu.cn
[1] State Key Laboratory of Material Processing and Die & Mold Technology, School of Materials Science and Engineering, Huazhong University of Science and Technology, Wuhan 430074, China
[2] Faculty of Engineering, China University of Geosciences, Wuhan 430074, China
Full list of author information is available at the end of the article

steel, Ti alloys, CoCrMo alloys, Cu alloys and Al alloys [12−16]. However, pure W is still difficult to fabricate using SLM due to its high melting point, high thermal conductivity, high viscosity and high DBTT, leading to pores formation and low-temperature brittleness. A limited number of studies pertaining to SLM W, most of which focused on enhancing the density and investigating the cracking phenomenon of SLM W parts, have been published. Zhang et al. [17] obtained a W part with a relative density of 82% by optimizing process parameters. When the laser energy density was below a certain threshold, metal powders could not be completely melted, resulting in lower relative density [18]. Zhou et al. [19] investigated the balling phenomena occurring during the SLM process. According to the cracking model of SLM W [20], the driving force of cracking was the thermal stress induced by the high temperature gradient during the SLM process. And cracks in SLM W appeared until the material was cooled to a threshold temperature according to the in situ observing by a high-speed camera [21]. Recently, SLM W parts with a higher relative density (more than 90%) were prepared by using finer W powders with spherical morphology, excellent flowability, suitable powder size and narrow particle size distribution [22−24].

Despite the advantages of the SLM in forming complex shapes and structures, the differences in the microstructure and macroscopic performance of pure W formed by SLM and that obtained using traditional methods are yet unclear. Further, it is not known if the SLM method can replace traditional methods in the field of nuclear materials. Research on these aspects has not been reported so far. Therefore, for the first time, a comparative research on the influence of different manufacturing methods (SLM and hot rolling) on the microstructure, mechanical and thermal behaviours of W was conducted. The purpose of this study is to evaluate the potential applications of SLM W in the nuclear industry.
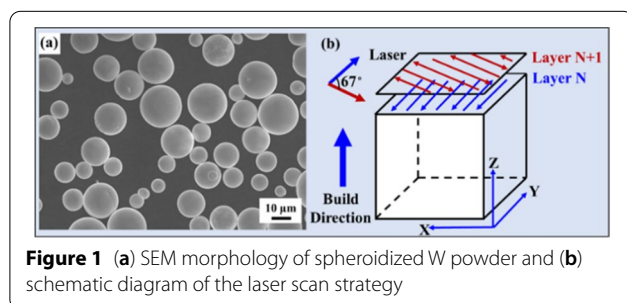
2 Experimental Procedure

2.1 Sample Preparation

Hot rolling W plate (Xiamen Tungsten Co. Ltd., Xiamen, China), manufactured by sintering and subsequent rolling at 1500 °C. Spherical W powder used for SLM was purchased from Tekna Advanced Materials Inc. (Quebec, Canada). The average particle size of W powder is 14.8 μm, as shown in Figure 1a.
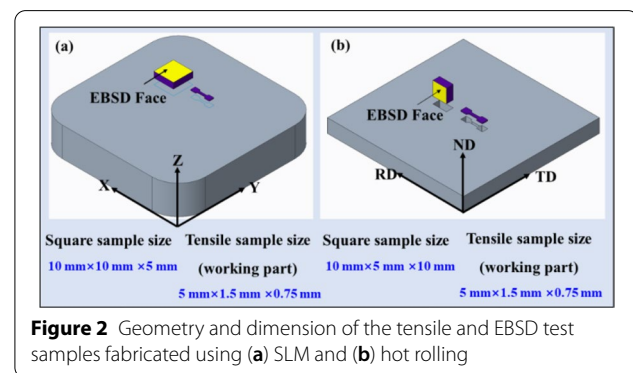
All the SLM W samples were fabricated on the SLM 125 machine. A cubic sample (10 mm × 10 mm × 5 mm) was prepared on a 316L steel substrate, which was maintained at 200 °C to reduce the thermal stress. The SLM process was carried out in an argon atmosphere to avoid oxidation. The laser scan strategy is shown in Figure 1b. In our previous work, the SLM process parameters, including the laser power, laser scanning speed, hatch spacing and layer thickness were optimized to obtain a part with the maximal density [19]. The optimized process parameters are shown in Table 1. The relative densities, as obtained using the Archimedes principle, of the samples prepared using hot-rolled and SLM were 97.4% and 98.7%, respectively.

2.2 Performance Testing

Figure 2 shows the geometry and dimension of test samples for microstructure and mechanical performance characterization. Before tensile test, all the samples were polished and cleaned to get fresh surface. The tensile direction of hot-rolled samples was the same as the rolling direction (RD), while the tensile direction of the

Table 1 SLM process parameters

Laser power (W)	Scan speed (mm/s)	Hatch spacing (μm)	Layer thickness (μm)
200	200	100	30

Figure 1 (**a**) SEM morphology of spheroidized W powder and (**b**) schematic diagram of the laser scan strategy

Figure 2 Geometry and dimension of the tensile and EBSD test samples fabricated using (**a**) SLM and (**b**) hot rolling

SLM samples was vertical to the building direction (BD). The high temperature tensile test was conducted on the Instron-5967 universal mechanical tester according to the standard ASTM E8M. The test temperature was from RT to 500 °C and tension rate was fixed at 0.6 mm/min.

A nano-indentation test was conducted using a Hysitron TI 750 (Bruker, American) nanoindenter with a load force of 7 mN for 5 s. At least five measurements were performed for each sample. The thermal conductivity (γ) of samples fabricated by SLM and hot rolling was calculated by the formula $\gamma = \alpha C_p \rho$. The thermal diffusivity (α) was measured using an LFA 427 (Nexus Analytics, Singapore) laser flash diffusivity system along the normal direction (ND) of the hot-rolled samples and *XY*-plane of the SLM samples. The density ρ of pure W is 19.3 g/cm^3. The specific heat C_p was obtained from Ref. [25].

2.3 Microstructure Characterization

The hot-rolled samples and SLM samples were prepared through wet grounding with SiC abrasive papers down to 2000 mesh to allow microstructural observation. Subsequently, the samples were polished with diamond suspensions and etched with a solvent containing of NaOH (10 g), K3 [Fe(CN)6] (10 g) and H_2O (100 mL) for 20 s. The microstructure was observed by optical microscope (OM) (ZEISS, Oberkochen, Germany). The phase identification was observed by an XRD-7000S instrument (Shimadzu, Japan) with a Cu tube at 40 kV and 30 mA. A scanning angle (2θ) ranging from 35° to 90° was employed with a continuous scan rate of 10°/min.

Average grain sizes and grain shape ratio were calculated according to Electron backscatter diffraction (EBSD) orientation maps. EBSD measurements were performed using a FEI Quanta 650 field-emission scanning electron microscope with an OIM orientation imaging microscope system (EDAX, Ametek, America). The EBSD data was processed using the HKL Channel 5 software packages. The samples for EBSD test were electrolytically polished with a 5% sodium hydroxide aqueous solution at 11 V and 30 mA/mm^2. Areas of 400×300 µm were scanned with a step size of 500 nm to analyse texture and microstructure.

3 Results and Discussion

3.1 Microstructure Characterization

Figure 3 shows the XRD patterns of the W powder, hot-rolled W and SLM W. The four observed diffraction peaks could be assigned to (110), (200), (211) and (220), as shown in Figure 3a. These results conformed to that of standard W diffraction with a body-centred cubic (bcc) lattice structure. Furthermore, the diffraction peak of SLM W was wider than those of hot-rolled W and W powder (Figure 3b), and this finding was
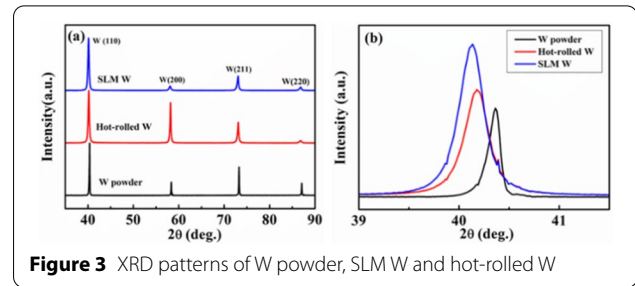

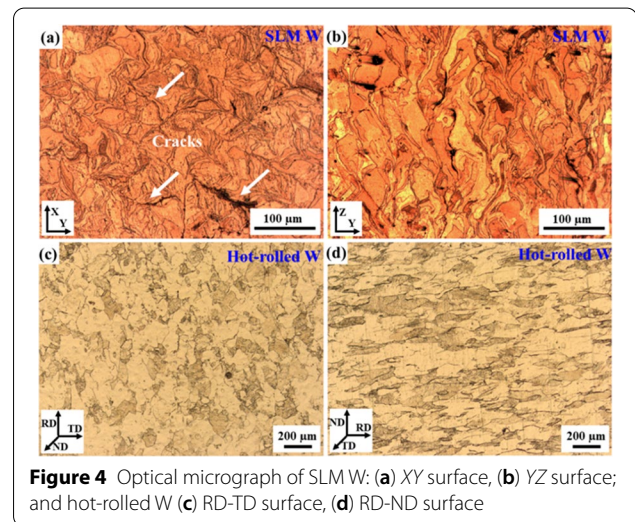**Figure 3** XRD patterns of W powder, SLM W and hot-rolled W

Figure 4 Optical micrograph of SLM W: (**a**) *XY* surface, (**b**) *YZ* surface; and hot-rolled W (**c**) RD-TD surface, (**d**) RD-ND surface

consistent with that of previous research [23]. According to the Debye-Scherrer formula, the peak broadening was related to the grain refinement, which was benefited by the rapid solidification during the SLM process. In addition, the main peaks shifted to the left also indicated the presence of high residual stress in the SLM W, resulting in lattice distortion [23, 26].

Furthermore, the (110) diffraction angle of SLM W gradually shifted to a lower angle compared to those of W powder and hot-rolled W, as shown in Figure 3b, and according to the Bragg equation as follows:

$$2d \sin\theta = \lambda, \tag{1}$$

where d is the interplanar spacing, θ is the diffraction angle and λ is the wavelength. According to Eq. (1), a smaller diffraction angle θ represents a larger interplanar spacing d, indicating the higher residual stress and lattice expansion of SLM W.

The optical micrograph surfaces of different directions of SLM W and hot-rolled W are shown in Figure 4. The individual scan tracks could be notably distinguished, and strip-shape grains were observed in

the *XY* surface of SLM W, as shown in Figure 4a. Longitudinal and transverse cracks were present, and they extended along the grain boundaries. Columnar grains were observed in the *YZ* surface, which were different from the strip-shape grains noted in the *XY* surface, as shown in Figure 4b. The columnar grains along the building direction are typical microstructure in the SLM of pure metals due to the maximum heat flow direction is parallel to building direction, leading to the epitaxial growth of grains [23]. As shown in Figure 4c and d, the hot-rolled sample demonstrated a notable fibre structure combined with the small recrystallized grains, which could be attributed to the dynamic recrystallization occurring during the hot rolling process [4]. Few micropores and micro-cracks could be observed in the hot-rolled W. The average grain size of the hot-rolled W was significantly larger than that of SLM W.

Figure 5a and b show the EBSD orientation maps of the hot-rolled W and SLM W. It can be found that the deformed grains extended along the RD, as shown in Figure 5a. The average length and width of the grains were approximately 74.6 μm and 34.8 μm, respectively. The grain shape aspect ratio was 2.14. A typical microstructure morphology of SLM W with striped-shape grains was observed, as shown in Figure 5b. Similar grain morphologies were also reported in previous studies [22, 23,

27]. The average grain size of SLM W was approximately 14.2 μm, which was considerably smaller than that of hot-rolled W. The finer grains of SLM W could be a result of the occurrence of rapid solidification with an extremely high cooling rate during the SLM process [8, 28].

To further characterize the crystallographic textures of hot-rolled W and SLM W, the pole figures and inverse pole figures are shown in Figure 5c to g. The texture of the hot-rolled W had the following characteristics: <110>//RD, <110>//TD, <111>//ND and <001>//ND. Zhang et al. [4] compared the macro-texture and mechanical properties of W prepared using different rolling methods and found that the main texture <001> and <111> was parallel to the ND, which is in agreement with our result. The main texture orientation of SLM W was the <111> direction, parallel to the building direction (*Z* axis) with a higher texture intensity of 4.9 compared to the corresponding value of approximately 3.9 for hot-rolled W. The *X* and *Y* directions of the inverse pole figure exhibited a similar texture orientation due to the continuous rotation laser scan [29], as shown in Figure 5g.

Figure 6a and b show the distribution of grain boundaries of hot-rolled W and SLM W, respectively. The differently coloured lines represented different grain boundary angles: sub-grain boundary (SGBs, 2°–5°, red), low angle grain boundary (LAGBs, 5°–15°, green), high-angle grain boundary (HAGBs, > 15°, blue). The distribution of the grain boundary misorientation angles of the hot-rolled W and SLM W are shown in Figure 6c. The hot-rolled W had a large number of LAGBs and SGBs, distributed inside the elongated grains. The similar sub-grain structures were also observed in other hot-rolled W, which were caused by plastic deformation [30]. During plastic
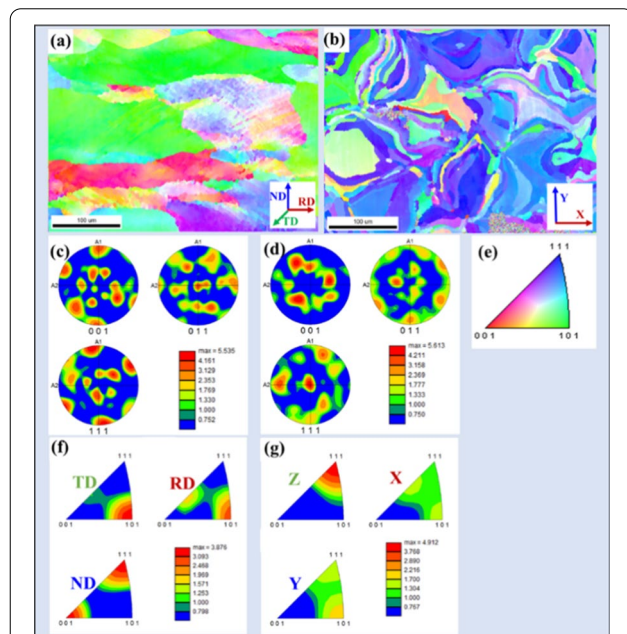

Figure 5 EBSD orientation maps of (**a**) hot-rolled W and (**b**) SLM W; pole figures of (**c**) hot-rolled W and (**d**) SLM W; (**e**) crystal orientation-colour relation map referred to the inverse pole figure; inverse pole figures of (**f**) hot-rolled W and (**g**) SLM W
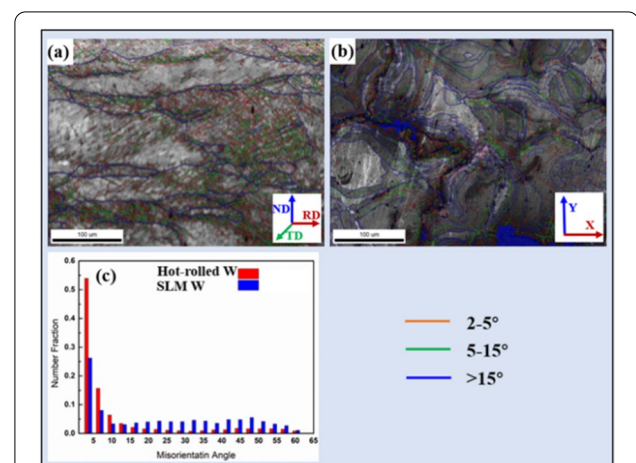

Figure 6 EBSD grain boundary maps of the (**a**) hot-rolled W and (**b**) SLM W; (**c**) distribution of misorientation angles of hot-rolled W and SLM W

Wang *et al. Chinese Journal of Mechanical Engineering*   (2022) 35:48

Page 5 of 8

deformation, low deformation temperature and high strain rate can introduce more dislocations and inhibit the dynamic recovery of dislocations, which is beneficial to the formation of dislocation walls and sub-grain. Compared with HAGBs, the misorientation of LAGBs is so small that dislocations are easier to transfer across the boundary of adjacent grains, reducing the dislocations pile-up [31, 32]. As a result, the SLM W with higher fraction of HAGBs exhibits better strain compatibility than hot-rolled W. HAGBs are the preferred crack paths because that grain boundaries with large misorientation can promote crack propagation and decrease fracture energy [33]. Therefore, hot-rolled W shows better ductility than SLM W according to the grain boundary analysis.
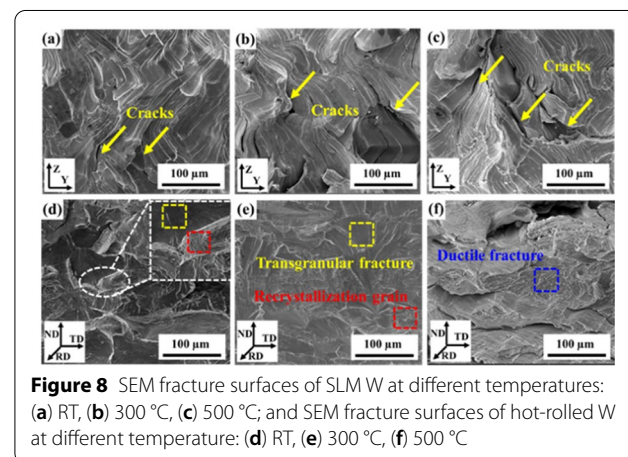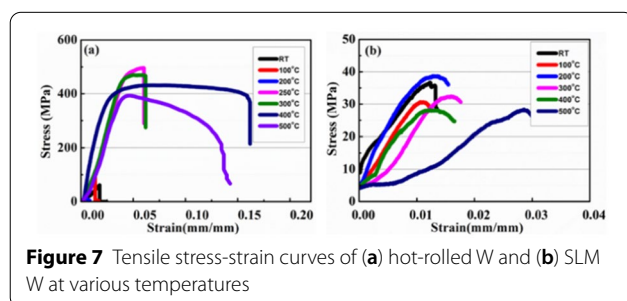
3.2 Mechanical and Thermal Properties

Figure 7 shows the tensile stress–strain curves of the hot-rolled W and SLM W at different temperatures. The tensile direction of the hot-rolled W was parallel to the RD. The hot-rolled W exhibited typical brittle fracture at RT, 100 °C and 200 °C. When the temperature increased to 250 °C, the ultimate tensile strength (UTS) of the hot-rolled W was 496 MPa and the total elongation (TE) was 6.0%. It is well known that the DBTT is defined as the lowest temperature at which a sample undergoes a minimum elongation beyond 5% without failure [34]. According to the high temperature tensile test, it could be estimated that DBTT of the considered hot-rolled W was approximately 250 °C, which was similar to the reported results [35]. With the temperature increased from 250 °C to 500 °C, the UTS decreased from 496 MPa to 393 MPa. Furthermore, the samples at 400 °C and 500 °C demonstrated considerably ductility with a TE of ~15%.

Figure 7b shows the tensile results of the SLM W at various temperatures. Even at the highest testing temperature of 500 °C, the SLM W exhibited almost no ductility and a rather low tensile strength. However, the compressive strength of the SLM pure W was approximately 1500 MPa, which was higher than coarse grain W (CG W) fabricated through powder metallurgy (PM) [5, 36]. Thus, it could be noted that SLM W exhibited an interesting performance involving a relatively high compressive strength and an extremely low tensile strength. According to our previous research [22], due to the high residual stress of the SLM process, some micro-cracks appear in the sample, resulting in the low plasticity of pure W at room temperature. Therefore, for the SLM W, the tensile properties were sensitive to the micro-cracks in the samples, while the compression properties were not sensitive. However, no effective method currently exists to eliminate the micro-cracks by adjusting the process parameters or adding toughening materials [37–39]. Compared with SLM W, hot-rolled W has been subjected to more uniform temperature, less thermal gradient and higher external pressure during hot rolling process, so hot-rolled W exhibits higher density and almost no pre-existing micro-cracks. According to the comparative study, suppressing micro-cracks and increasing strength will be a research hotspot of SLM W.

Figure 8 shows the fracture surfaces of the SLM W and hot-rolled W at different test temperatures. The pre-existing micro-cracks acted as the source of cracks propagation, as shown in Figure 8a to c. Under tensile loading, the micro-cracks grew along the grain boundaries. According to Figure 4a and b, a large number of micro-cracks were distributed along the grain boundaries, which significantly weakened the bonding strength between the neighbouring grains. Thus, the fracture surfaces of SLM W were dominated by intergranular fracture, which propagated along the strip-shaped grain boundaries. Figure 8d shows that the fracture surfaces of hot-rolled W at room temperature were dominated by transgranular fracture (green dotted rectangles). Some intergranular fracture was also present along the rolling direction (red dotted rectangles), in which a fine and equiaxed recrystallization microstructure was observed. As shown in Figure 8e, the sample demonstrated a
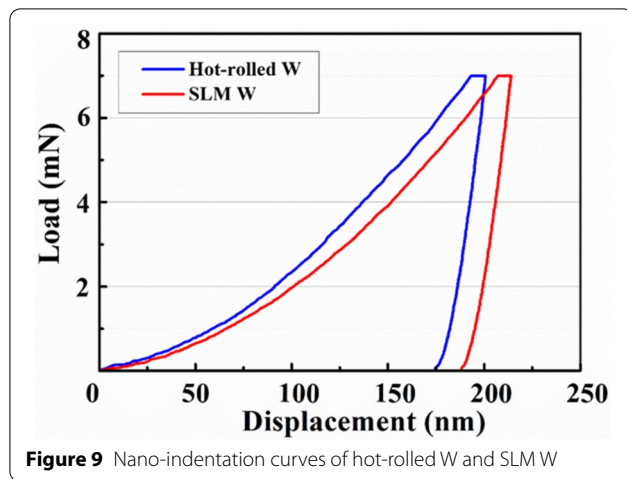

Figure 7 Tensile stress-strain curves of (**a**) hot-rolled W and (**b**) SLM W at various temperatures

Figure 8 SEM fracture surfaces of SLM W at different temperatures: (**a**) RT, (**b**) 300 °C, (**c**) 500 °C; and SEM fracture surfaces of hot-rolled W at different temperature: (**d**) RT, (**e**) 300 °C, (**f**) 500 °C

Wang *et al. Chinese Journal of Mechanical Engineering*   (2022) 35:48

Page 6 of 8

Figure 9 Nano-indentation curves of hot-rolled W and SLM W

smaller cleavage surface and exhibited a certain amount of ductility. Nevertheless, at 500 °C the hot-rolled samples exhibited extremely ductile in Figure 8f. Strong necking phenomenon and many dimples can be observed on the fracture surfaces.

To further study the influence of micro-cracks on the mechanical performance of the hot-rolled W and SLM W, nano-indentation test was carried out. As shown in Figure 9, the load–depth curves of SLM W and hot-rolled W were present. Three segments were observed in the curves: loading, holding at maximum load and unloading. A larger depth was observed for SLM W at the same load, demonstrating that SLM W exhibited a lower hardness than hot-rolled W. In this work, the Oliver-Pharr analysis [40] was applied to calculate the hardness and elastic modulus. The hardness (H) is defined as follows [12, 41]:

$$H = \frac{P_{\max}}{A_c} \qquad (2)$$

$$A_c = f\left(h_c{}^2\right) = 24.5 h_c{}^2 \qquad (3)$$

where $P_{\max}$ is the maximum load, A_c is the area of the indentation, h_c is the contact depth at the maximum load. It could be determined that the hardness of the hot-rolled W (5.85 ± 0.18 GPa) was slightly higher than that of SLM W (5.51 ± 0.24 GPa). The results were in accordance with those presented in previous reports, indicating the results were reliable [37, 42]. It could be concluded that the rolled W was harder than the SLM W. Furthermore, the curves of hot-rolled W and SLM W demonstrated a similar unloading segment, implying a similar elastic modulus.

Even though the grain size of SLM was smaller, hot-rolled W exhibited higher nano-hardness and tensile

strength. It could be speculated that the SLM W samples had large numbers of micro-cracks, which could easily expand. This W was sensitive to cracking, because of its high DBTT (~ 400 °C) [36]. The cracking of W was difficult to suppress due to the high thermal stress, which was larger than the intrinsic ductility. Wang et al. [35] reported that the segregated nano-pores at the grain boundaries (GBs) acted as crack nucleation zones.

The thermal conductivities of the hot-rolled W, SLM W, SPS W and ITER grade W are shown in Figure 10. At room temperature, the thermal conductivity of hot-rolled W was 182 W/m·K, that was 23% higher than that of SLM W. As is well known, the thermal conductivity was dependent on many factors, for instance the relative density, grain size, grain shape, grain boundary, defect and porosity. The relative density of the hot-rolled W and SLM W was 97.4% and 98.7%, respectively. The grain size of the hot-rolled W along the ND was 34.8 μm, which was approximately 2.5 times that of the SLM W. The GB density of the hot-rolled W was significantly less compared with that of the SLM due to larger average grain size of hot-rolled W. When there are more grain boundaries, the electrons are more likely to scatter at the interface and thus reduce thermal conductivity. At the same time, the SLM W exhibited a higher thermal conductivity compared with SPS W, because the columnar grain of the SLM W along the building direction was conducive to the thermal conduction [25].

4 Conclusions
A comparative research on the influence of different manufacturing methods (SLM and hot rolling) on the microstructure, mechanical and thermal behaviours of W was conducted. The SLM W exhibited a smaller average grain
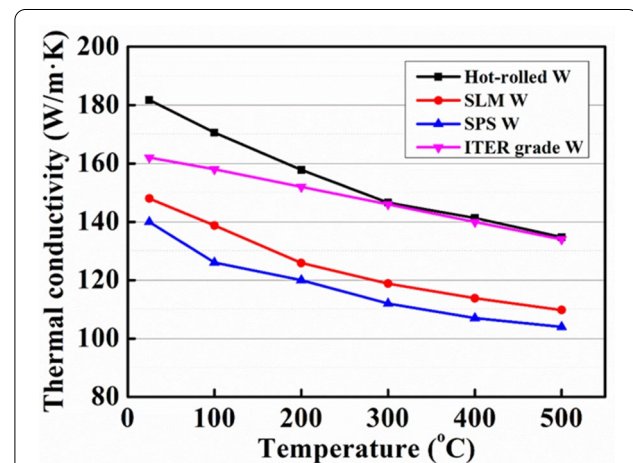

Figure 10 Thermal conductivity of hot-rolled W, SLM W, SPS W [25] and ITER grade W [43]

Wang *et al. Chinese Journal of Mechanical Engineering*   (2022) 35:48

Page 7 of 8

size (14.2 μm) due to the high solidification rate of the laser process. While the hot-rolled W exhibited a finer equiaxed recrystallizing sub-grain microstructure. The hot-rolled W demonstrated the best performance in terms of the tensile strength (496 MPa at 250 °C), nano-hardness (5.85 ± 0.18 GPa) and thermal conductivity (182 W/m·K).

Acknowledgements

Authors' Information
Chong Wang, born in 1995, is a master candidate at *State Key Laboratory of Material Processing and Die & Mold Technology, Huazhong University of Science and Technology, China.*

Yan Zhou, born in 1987, is an associate professor at *Faculty of Engineering, China University of Geosciences (Wuhan), China.*

Shifeng Wen, born in 1979, is an associate professor at *State Key Laboratory of Material Processing and Die & Mold Technology, Huazhong University of Science and Technology, China.*

Author Contributions
SW and QF designed the experiment; CW and DC were in charge of the whole trial; CW and YZ wrote the manuscript; ZX and CY assisted with sampling and laboratory analyses. All authors read and approved the final manuscript.

Funding

Competing Interests
The authors declare no competing financial interests.

Author Details
[1] State Key Laboratory of Material Processing and Die & Mold Technology, School of Materials Science and Engineering, Huazhong University of Science and Technology, Wuhan 430074, China. [2] Faculty of Engineering, China University of Geosciences, Wuhan 430074, China. [3] Key Laboratory of Materials Physics, Institute of Solid State Physics, Chinese Academy of Sciences, Hefei 230031, China.

References
[1] E Lassner, W Schubert. *Tungsten: Properties, chemistry, technology of the element, alloys, and chemical compounds*. New York: Kluwer Academic, 1999.
[2] J Knaster, A Moeslang, T Muroga. Materials research for fusion. *Nature Physics*, 2016, 12: 424-434.
[3] P Gumbsch, J Riedle, A Hartmaier, et al. Controlling factors for the brittle-to-ductile transition in tungsten single crystals. *Science*, 1998, 282(5392): 1293-1295.
[4] X Zhang, Q Yan, S Lang, et al. Preparation of pure tungsten via various rolling methods and their influence on macro-texture and mechanical properties. *Materials & Design*, 2017, 126: 1-11.
[5] S Bonk, J Hoffmann, A Hoffmann, et al. Cold rolled tungsten (W) plates and foils: Evolution of the tensile properties and their indication towards deformation mechanisms. *International Journal of Refractory Metals and Hard Materials*, 2018, 70: 124-133.
[6] J K Lee, S Y Kim, R T Ott, et al. Effect of reinforcement phase on the mechanical property of tungsten nanocomposite synthesized by spark plasma sintering. *International Journal of Refractory Metals and Hard Materials*, 2016, 54: 14-18.
[7] D Hancock, D Homfray, M Porton, et al. Exploring complex high heat flux geometries for fusion applications enabled by additive manufacturing. *Fusion Engineering and Design*, 2018, 136: 454-460.
[8] S Wen, K Chen, W Li, et al. Selective laser melting of reduced graphene oxide/S136 metal matrix composites with tailored microstructures and mechanical properties. *Materials and Design*, 2019, 175: 107811.
[9] J Zhang, B Song, Q Wei, et al. A review of selective laser melting of aluminum alloys: Processing, microstructure, property and developing trends. *Journal of Materials Science & Technology*, 2019, 35(2): 270-284.
[10] S A Yavari, J van der Stok, Y C Chai, et al. Bone regeneration performance of surface-treated porous titanium. *Biomaterials*, 2014, 35(24): 6172-6181.
[11] M Leary, M Mazur, J Elambasseril, et al. Selective laser melting (SLM) of AlSi12Mg lattice structures. *Materials & Design*, 2016, 98: 344-357.
[12] W Li, Y Yang, J Liu, et al. Enhanced nanohardness and new insights into texture evolution and phase transformation of TiAl/TiB2 in-situ metal matrix composites prepared via selective laser melting. *Acta Materialia*, 2017, 136: 90-104.
[13] C Han, C Yan, S Wen, et al. Effects of the unit cell topology on the compression properties of porous Co-Cr scaffolds fabricated via selective laser melting. *Rapid Prototyping Journal*, 2017, 23(1): 16-27.
[14] S Wen, H Hu, Y Zhou, et al. Enhanced hardness and wear property of S136 mould steel with nano-TiB2 composites fabricated by selective laser melting method. *Applied Surface Science*, 2018, 457: 11-20.
[15] Y Zhou, X Zeng, Z Yang, et al. Effect of crystallographic textures on thermal anisotropy of selective laser melted Cu-2.4Ni-0.7Si alloy. *Journal of Alloys and Compounds*, 2018, 743: 258-261.
[16] M B Wang, R D Li, T C Yuan, et al. Microstructures and mechanical property of AlMgScZrMn-A comparison between selective laser melting, spark plasma sintering and cast. *Materials Science & Engineering A*, 2019, 756: 354-364.
[17] D Zhang, Q Cai, J Liu. Formation of nanocrystalline tungsten by selective laser melting of tungsten powder. *Materials and Manufacturing Processes*, 2012, 27(12): 1267-1270.
[18] R K Enneti, R Morgan, S V Atre. Effect of process parameters on the selective laser melting (SLM) of tungsten. *International Journal of Refractory metals and Hard Materials*, 2017, 71: 315-319.
[19] X Zhou, X Liu, D Zhang, et al. Balling phenomena in selective laser melted tungsten. *Journal of Materials Processing Technology*, 2015, 222: 33-42.
[20] D Z Wang, K L Li, C F Yu, et al. Cracking behavior in additively manufactured pure tungsten. *Acta Metallurgica Sinica (English Letters)*, 2019, 32(1): 127-135.
[21] B Vrancken, W King, M Matthews. In-situ characterization of tungsten microcracking in selective laser melting. *Procedia CIRP*, 2018, 74: 107.
[22] S Wen, C Wang, Y Zhou, et al. High-density tungsten fabricated by selective laser melting: Densification, microstructure, mechanical and thermal performance. *Optics & Laser Technology*, 2019, 116: 128-138.
[23] C Tan, K Zhou, W Ma, et al. Selective laser melting of high-performance pure tungsten: Parameter design, densification behavior and mechanical properties. *Science and Technology of Advanced Materials*, 2018, 19(1): 370–380.
[24] D Wang, C Yu, X Zhou, et al. Dense pure tungsten fabricated by selective laser melting. *Applied Sciences*, 2017, 7(430): 1-13.
[25] Z M Xie, R Liu, S Miao, et al. High thermal shock resistance of the hot-rolled and swaged bulk W-ZrC alloys. *Journal of Nuclear Materials*, 2016, 469: 209-216.
[26] B Li, B Qian, Y Xu, et al. Additive manufacturing of ultrafine-grained austenitic stainless steel matrix composite via vanadium carbide reinforcement addition and selective laser melting: Formation mechanism and strengthening effect. *Materials Science and Engineering: A*, 2019, 745: 495-508.
[27] A Ivekovic, N Omidvari, B Vrancken, et al. Selective laser melting of tungsten and tungsten alloys. *International Journal of Refractory Metals and Hard Materials*, 2018, 72: 27-32.
[28] B Song, X Zhao, S Li, et al. Differences in microstructure and properties between selective laser melting and traditional manufacturing for fabrication of metal parts: A review. *Frontiers of Mechanical Engineering*, 2015, 10(2): 111-125.
[29] M Cloots, P J Uggowitzer, K Wegener. Investigations on the microstructure and crack formation of IN738LC samples processed by selective laser

melting using Gaussian and doughnut profiles. *Materials & Design*, 2016, 89: 770-784.

[30] S Miao, Z M Xie, L F Zeng, et al. Mechanical properties, thermal stability and microstructure of fine-grained W-0.5 wt.% TaC alloys fabricated by an optimized multi-step process. *Nuclear Materials and Energy*, 2017, 13: 12-20.

[31] D Rupp, R Monig, P Gruber, et al. Fracture toughness and microstructural characterization of polycrystalline rolled tungsten. *International Journal of Refractory Metals and Hard Materials*, 2010, 28(6): 669-673.

[32] Z M Xie, S Miao, T Zhang, et al. Recrystallization behavior and thermal shock resistance of the W-1.0 wt% TaC alloy. *Journal of Nuclear Materials*, 2018, 501: 282-292.

[33] T Shen, Y Dai, Y Lee. Microstructure and tensile properties of tungsten at elevated temperatures. *Journal of Nuclear Materials*, 2016, 468: 348-354.

[34] T Dummer, J C Lasalvia, G Ravichandran, et al. Effect of strain rate on plastic flow and failure in polycrystalline tungsten. *Acta Materialia*, 1998, 46(17): 6267-6290.

[35] D Wang, Z Wang, K Li, et al. Cracking in laser additively manufactured W: Initiation mechanism and a suppression approach by alloying. *Materials & Design*, 2019, 162: 384-393.

[36] D Z Wang, K L Li, C F Yu, et al. Cracking behavior in additively manufactured pure tungsten. *Acta Metallurgica Sinica (English Letters)*, 2018, 32: 127-135.

[37] K Li, D Wang, L Xing, et al. Crack suppression in additively manufactured tungsten by introducing secondary-phase nanoparticles into the matrix. *International Journal of Refractory Metals and Hard Materials*, 2019, 79: 158-163.

[38] Y Cheng, M Mrovec, P Gumbsch. Atomistic simulations of interactions between the 1/2(111) edge dislocation and symmetric tilt grain boundaries in tungsten. *Philosophical Magazine*, 2008, 88(4): 547-560.

[39] C Ren, Z Z Fang, L Xu, et al. An investigation of the microstructure and ductility of annealed cold-rolled tungsten. *Acta Materialia*, 2019, 162: 202-213.

[40] W C Oliver, G M Pharr. An improved technique for determining hardness and elastic modulus using load and displacement sensing indentation experiments. *Journal of Materials Research*, 2011, 7(6): 1564–1583.

[41] H Attar, S Ehtemam-Haghighi, D Kent, et al. Nanoindentation and wear properties of Ti and Ti-TiB composite materials produced by selective laser melting. *Materials Science and Engineering: A*, 2017, 688: 20-26.

[42] D E J Armstrong, T B Britton. Effect of dislocation density on improved radiation hardening resistance of nano-structured tungsten-rhenium. *Materials Science and Engineering A*, 2014, 611: 388-393.

[43] G Pintsuk, H Kurishita, J Linke, et al. Thermal shock response of fine- and ultra-fine-grained tungsten-based materials. *Physica Scripta*, 2011, T145: 014060.